CrystEngComm

Spherulite-enhanced Macroscopic Polarization in Molecular Ferroelectric Films from Vacuum Deposition

Journal:	*CrystEngComm*
Manuscript ID	CE-ART-04-2024-000417.R1
Article Type:	Paper
Date Submitted by the Author:	05-Jun-2024

Complete List of Authors:	Tiwari, Bibek; University of Nebraska-Lincoln, Physics & Astronomy Ni, Yuanyuan; University of Nebraska-Lincoln, Physics & Astronomy Savage, Jackson; University of Illinois Chicago Department of Physics, Department of Physics Daugherty, Ellen; The College of Wooster Department of Chemistry, Department of Chemistry Giri, Bharat; University of Nebraska-Lincoln, Physics & Astronomy Li, Xin; University of Nebraska-Lincoln, Physics & Astronomy Xu, Xiaoshan; University of Nebraska-Lincoln, Physics and Astronomy

SCHOLARONE™
Manuscripts

Data available on request from the authors.

Spherulite-enhanced Macroscopic Polarization in Molecular Ferroelectric Films from Vacuum Deposition

Bibek Tiwari[1], Yuanyuan Ni[1], Jackson Savage[2], Ellen Daugherty[3], Bharat Giri[1], Xin Li[1], and Xiaoshan Xu[1,4*]

[1]*Department of Physics and Astronomy, University of Nebraska-Lincoln, Nebraska 68588, USA*

[2]*Department of Physics, University of Chicago, Illinois 60637, USA*

[3]*Department of Chemistry, The College of Wooster, Ohio 44691, USA*

[4]*Department of Physics and Astronomy and the Nebraska Center for Materials and Nanoscience, University of Nebraska-Lincoln, Lincoln, Nebraska 68588, USA*

*xiaoshan.xu@unl.edu

Abstract:

Proton-transfer type molecular ferroelectrics hold significant promise for practical application due to their large spontaneous polarizations, high Curie temperatures, and small switching fields. However, it remains puzzling that preparation of quasi-2D films exhibiting macroscopic ferroelectric behaviors has been reported in only few molecular ferroelectrics. To address this puzzle, we studied the impact of microstructures on the macroscopic ferroelectric properties of 5,6-Dichloro-2-methylbenzimidazole (DC-MBI) films grown using the low-temperature deposition followed by restrained crystallization (LDRC) method. Our findings revealed a competition between dense spherulites and porous microstructures containing randomly oriented nanograins in the as-grown films. Post-growth annealing at moderate temperature promotes the formation of spherulites, leading to macroscopic ferroelectric polarization switching. These results underscore the critical role of microstructure density in determining macroscopic ferroelectric properties, potentially resolving the puzzle for absence of such behavior in many molecules ferroelectric films. We anticipate the approach proposed in this study to enhance microstructure density will significantly advance the fabrication of quasi-2D molecular ferroelectrics films and unlock their potential in device applications.

Keywords: Organic Ferroelectrics, Hydrogen-bonded, DC-MBI, Physical vapor deposition, thin film

I. Introduction

The potential benefit of utilizing organic ferroelectric materials carry significant implications across various applications. Notably, their remarkable dielectric, pyroelectric, and piezoelectric properties, on par with those observed in conventional inorganic ferroelectrics, position them as promising contender for roles in actuators, transducers and pyroelectric detectors[1–4]. Moreover, their environmentally friendly attributes stand in stark contrast to the prevalent use of lead and rare-metal ferroelectrics in today's technology landscape.

Proton-transfer type ferroelectrics of molecular crystals, compared with other organic ferroelectrics, offer distinct advantages, including low coercivity (~10 kV/cm) and large spontaneous polarizations[5]. In particular, croconic acid exhibits spontaneous polarizations around 30 μC/cm^2, [6] which is on par with prototype inorganic ferroelectric $BaTiO_3$. The presence of hydrogen bonds, responsible for cohesion in proton-transfer molecular ferroelectrics, allows spontaneous polarization to persists up to the melting temperature, typically exceeding 400 K[5,7,8], which is comparable to the Curie temperature of $BaTiO_3$.

The application potential of organic ferroelectrics hinges on viable thin-film fabrication approaches that preserve their ferroelectric properties. However, the growth of quasi-2D films of molecular ferroelectrics seems to conflict with the crystallization process[9,10], which is essential establishing ferroelectric order. The conflict arises because molecular crystals tend to form 3D structures due to their weak interactions with most inorganic substrates. Recently, a method called low-temperature deposition followed by restrained crystallization (LDRC) has emerged as a promising route. It allows control over film crystallization while maintaining the quasi-2D morphology. For instance, when applied to methyl-benzimidazole (MBI)[11], LDRC results in quasi-2D highly-oriented dense spherulites that exhibit single-crystal-level ferroelectric properties. On the other hand, croconic acid films typically consist of porous microstructures with randomly oriented nanograins[12]. Although ferroelectric polarization switching has been routinely demonstrated for individual grains[13,14], achieving it with macroscopic electrodes in croconic acid films remains rare[15]. Therefore, beyond considering quasi-2D morphology and crystallization, understanding the optimal microstructure for ferroelectric behavior and developing strategies to achieve it are critical questions.

To address these questions, we turn our attention to 5,6-Dichloro-2-methylbenzimidazole (DC-MBI), a proton-transfer type ferroelectric with spontaneous polarization approximately 10 μC/cm^2 (at 373 K)[6,16]. As shown in **Fig. 1(a)**, DC-MBI crystallizes in a $Pca2_1$ structure in which the molecules form a chain-like structure connected by the N-H··N hydrogen bonds[6]. The spontaneous polarization is along the *c* axis, which corresponds to the chain direction. Note that the melting point of DC-MBI is about 250 °C, positioning it between that of MBI (≈ 175 °C) and croconic acid (≈ 300 °C)[17–19]. Therefore, we anticipate that DC-MBI films will exhibit microstructure characteristics from both MBI (dense spherulites) and croconic acid (porous randomly oriented nanograins). Indeed, employing the LDRC method [**Fig. 1(b)**], we observe a competition between spherulites and porous microstructure of randomly oriented nanograins. Furthermore, post-deposition annealing at moderate temperature promotes the formation of

spherulites, resulting in well-defined ferroelectric switching loops and enhanced dielectric constants.

II. Results and Discussions

Growth of DC-MBI films

We first determine the effect of substrate temperature on the formation of spherulites. **Figs. 2(a-f)** show the laser microscopy images for the DC-MBI films (for powder sample morphology via SEM and TEM, see **Fig. S1**). These films were deposited on sapphire substrates in high vacuum, with various substrate temperatures T_s with nominal thickness 1 μm. The warming process was gradual (~ 0.2 K per minute) until reaching room temperature. At T_s = 294 K [**Fig. 2(a)**], the most prominent features in the image are the disk-shaped structures (highlighted by the box). These disks have an approximate diameter of 100 μm and a thickness of 1.0 ± 0.6 μm (for statistics at other T_s see Table S1 in supplementary). We refer to these as Type-I features. In addition, dendric-shaped features are visible. Notably, the large white area in the image remains uncovered by the film. As we decrease T_s to ≤273 K, another disk-shaped feature emerges alongside Type-I. This one has a thickness of 2.0 ± 1.2 μm. We label it Type-II (see **Fig. 2(b)**). When T_s drops below 173 K, both Type-I and Type-II features persist, but the substrates become fully covered, as indicated by the extensive grey area. **Fig. 2(g)** shows the area coverage as functions of thickness. Overall, coverage of both Type-I and Type-II features diminishes for both low and high T_s. Interestingly, the maximum coverage for the Type-II occurs at higher T_s compared to that of the Type-I.

The Type-I feature appears to be spherulites. **Fig. 2(h)** provides a closed-up view of the Type-I feature in **Fig. 2(b)**. On top of the circular shape are ring-like bands evenly spaced around the center, following a radial direction. These rings are a typical characteristic of spherulites resulting from rhythmic growth[20,21]. On the other hand, the Type-II feature in **Fig. 2(i)**, while also circular, appears more porous, with fluffy boundaries and lacking the distinct rings, which is consistent with spherical dendrites[22]. The ordered nature of the Type-I feature is further confirmed by the scanning electron microscopy (SEM) images shown in **Fig. S2**. In contrast, the background grey area in **Fig. 2(f)** shows no sign of order.

The T_s dependence of the images in **Fig. 2(a-f)** can be understood in terms of spherulite and dendrite nucleation. When T_s is below 173 K, the sticking coefficient[23] during the deposition is high, resulting in full film coverage. Nucleation of spherulites and dendrites occurs as the films warm up to room temperature. The disk shape arises due to the constraint imposed by the film morphology during the low temperature deposition[11]. Conversely, when T_s exceeds 173 K, the sticking coefficient decreases. The reduction means that nucleation of spherulites and dendrites is important for the film coverage. Typically, spherulite growth requires large supersaturation and slow growth speed[21] compared to the dendrites. This is consistent with the observation that the T_s for maximum coverage of the spherulite is lower than with that for spherical dendrites in **Fig. 2(g)**. Therefore, we decided that the optimal substrate temperature for promoting the spherulites growth is T_s =183 K.

Next, we study the effect of film thickness at substrate temperature T_s of 183 K. To assess the ferroelectric properties, the substrates were pre-patterned with Pt interdigital electrodes (IDE). **Figs. 3(a-d)** display the optical images for films on IDE (similar morphology observed on Au/Si substrate, **Fig. S3**) with crossed polarizers of various film thicknesses. In this setup, the light path involves the 1st polarizer, the film, followed by the 2nd polarizer. When the film is optically isotropic, no light passes through the 2nd polarizer, resulting in a dark image. On the other hand, if the film has in-plane anisotropy, it can rotate the light polarization, leading to non-zero transmission through the 2nd polarizer, unless the light's polarization aligns precisely with the film's optical axis. Spherulites consists of fiber crystallites aligned radially. The optical axes predominantly run parallel or perpendicular to the fiber, causing rotation of light's polarization, except when the radial direction aligns with either polarizer's axis. This phenomenon gives rise to the characteristic Maltese cross, a hallmark feature of spherulites[21], as clearly observed for the Type-I feature in **Figs. 3(a-d)**. Here the axes of the maximum intensity form a 45° angle with both polarizers' axes. In contrast, the Type-II feature exhibits substantially weaker light intensity than the Type-I feature and lacks the Maltese cross. This aligns with its less-ordered structure. Finally, the backgrounds area, referred to as the Type-III feature, shows minimal light intensity, indicative of a highly disordered nature. Additionally, the XPS measurement (**Fig. S4)** qualitatively reveals a similar bonding environment for both the powder and film samples.

We confirm the microstructure order of these features using atomic force microscopy (AFM), as depicted in **Figs. 3(e-g).** In these images, one can discern the step (approximately 200 nm) and the periodicity (around 10 μm) of the IDE. From Type-I to Type-III, the disorder increases. Type-I feature [**Fig. 3(e)**] consists of well-aligned crystallite fibers densely packed together. In comparison, in the Type-II feature [**Fig. 3(f)**], the fibers are less aligned, resulting in a porous structure. However, there is still a discernable alignment direction in the image. For the Type-III area [**Fig. 3(g)**], the fibers are randomly oriented, leading to even greater porosity. As a consequence, the area becomes optically isotropic, consistent with the minimal light intensity observed for the Type-III feature in **Figs. 3(a-d)**. Additionally, we can infer the disorders and porosity from the roughness of the AFM images measured within the IED digits. Specifically, the root-mean-square roughness is approximately 30 nm, 70 nm, and 100 nm for the Type-I, Type-II, and Type-III regions respectively. Therefore, there is a clear correlation between the brightness observed in the crossed-polarizer optical images, the microstructure density/porosity, and the order of the crystallite fibers.

Fig. 3(h) shows how the coverage of the different feature types depends on film thickness. As the thickness increases, the coverage of the Type-II feature increases monotonically, while the Type-III area consistently reduces. In particular, at 4 μm thickness, the majority of the area is occupied by both Type-I and Type-II features, with the less-ordered type-II feature prevailing.

Annealing and Electrical Study of the films

Previous work on MBI[11] revealed that single-crystal-level ferroelectric properties were obseved in films consisting of spherulites. To increase the population of spherulites, which is the most ordered microstructures among the three types of feature, we carried out annealing on the film samples. During this process, the sample were gradually (approximately 0.2 K per minute)

warmed up in the atmosphere from room temperature to 353 K and kept at 353 K for 2.5 hours. **Figs. 4(a&b)** are optical images (from different areas) of a 4 μm film before and after the annealing, respectively, with crossed polarizers. After the annealing, most area in the image is covered by the Maltese cross, indicating dominance by the Type-I feature (spherulites). In other words, the presence of the Type-II and Type-III features was significantly reduced. Additionally, the Maltese crosses observed after the annealing [**Fig. 4(b)**] are often much larger than those before annealing [**Fig. 4(a)**], approaching the sizes of the Type-II features in **Fig. 4(a)**. This suggests that the Type-II feature may have achieved better fiber order and transformed into spherulite similar to the Type-I feature. Further insight into the annealing effect can be gleaned from AFM images. **Fig. 4(c)** shows an area of densely packed fibers in the Type-I feature. After the annealing [**Fig. 4(d)**], the fibers appeared noticeably longer, likely due to merging. More importantly, the alignment (or order) became more obvious.

Specular θ-2θ x-ray diffraction (XRD) provides insights into the preferred crystalline orientations of the films (for comparison with powder and simulation, see **Fig. S1d**). These orientations clearly changes with thickness, as shown in **Fig. 4(e)**. For the 1 μm film, despite the weak diffraction intensity, the most well-defined peaks are (210) and (311). Interestingly, the (010) peak, nearly invisible for the power sample, is now discernable. Consequently, for the 1 μm film, the (010) direction appears to be the preferred out-of-plane direction. The (010) peak becomes well-defined for the 2 μm and 3 μm films, although the relative intensity decreases with the film thickness. For the 4 μm film, the (010) peak disappears. In contrast, the (002) peak, initially very weak in the powder sample, grows stronger with the film thickness. This suggests that the (001) orientation is preferred for the thicker films. For the 4 μm film after annealing, the (002) peak still is strong, maintaining the (001) as the preferred orientation.

Therefore, annealing clearly enhances the order of the crystallite fibers and overall density of the microstructure. This improvement is anticipated to positively impact the macroscopic ferroelectric properties of the DC-MBI films, as discussed below.

The in-situ measurement of polarization-voltage (P-V) relation sheds light on how microstructure impacts the macroscopic ferroelectric properties. At T_s = 183 K, the P-V relation is linear (for comparion with different thickness, see **Fig. S5**), indicating behavior akin to a typical capacitor. In **Fig. 5(a)**, the capacitances are plotted as functions of thickness for various films. The analysis based on partial capacitance model[24] results in dielectric constants $\epsilon_{DC\text{-}MBI}$ = 2.7 for DC-MBI and $\epsilon_{Substrate}$ = 5.4 for the IDE. Notably, the value for DC-MBI is close to that of amorphous MBI (2.93)[11], which is a factor of 30 less than the value for MBI single crystals. Therefore, DC-MBI films at T_s =183 K is most likely in an amorphous phase.

The effect of annealing (0.2 K per minute from room temperature to 353 K) becomes evidence in **Fig. 5(b)** for a 4 μm film. Before annealing, the P-V relation at room temperature (294 K) has a visible but minimal opening, attributed to the limited order shown in **Fig. 5(b)**. After annealing at 353 K for 2.5 hours, the loop opens further. This suggests that the transformation from more disordered microstructures to spherulites drives the macroscopic ferroelectric behavior in DC-MBI (for local microscopic ferroelectric domain and poling results, see **Fig. S6 and Fig. S7**). Even upon cooling back to room temperature (294 K), the P-V loop remains open, confirming that

this behavior primarily arises from the irreversible process of microstructure ordering. The remanent polarization at 294 K after cooling, measured using the PUND method at 0.5 Hz for the 4 μm thick sample, is approximately 0.2 μC/cm²,.

The current-voltage (I-V) relationship in **Fig. 5(c)**, along with the resistance measured at 150 V (**Fig. 6**), reveals a large change of resistance at transition temperature. During the deposition at T_s = 183 K, the I-V relation is linear but with a small slope. This corresponds to large (approximately 100 GΩ) resistance of the insulating dielectrics between IDEs. As the film warms up, the I-V relation ehxibits current peaks superimposed on a linear background. These current peaks are consistent with the polarization switching; the slope of the linear background is the inverse of resistance, which decreases during the annealing procecess. At 353 K after 2.5 hours annealing, the resistance drops to approximately 1 GΩ, a two-orders-of-magnitude decrease compared to the value at 183 K for the amorphous phase. However, the subtle structrual transition occurs at ~293K, as indicated by capacitance, resistance, and remenance measurements (**Fig. 6**). Here, the resistance drops to approximately 7 GΩ. This large resistance change is consistent with the amorphous-to-spherulite transition observed in MBI films. After cooling down to 294 K and below, the resistance remains consistently low (≈ 10 GΩ), confirming the irreversible microstructure ordering process.

Discussion:

The formation of spherulites in thin films depends on two critical conditions: (1) large driving force which can result from supercooling or super saturation, and (2) slow kinetics due to interface-controlled growth[21]. The large driving force can be realized at low deposition temperature, which is also necessary for (1) reducing the diffusion so that a quasi-2D morphology can be formed and (2) increasing the sticking coefficient so that high film coverage can be achieved.

On the flip side, using a low deposition temperature may significantly slow down the spherulite growth to an impractical time scale. Consequently, post-deposition annealing becomes essential. The optimal annealing temperature is determined by the crystal growth speed which reaches a maximum at an intermediate temperature T_{max}. This maximum occurs because growth is slow both at low temperature (due to the slow diffusion) and at high temperature (due to the small driving force). Previous work indicates that $T < T_{max}$ favors spherulite growth, while $T > T_{max}$ promotes larger 3D single crystals[21]. Hence, the annealing temperature should satisfy $T < T_{max}$. In this work, besides the annealing described in **Fig. 5** and **Fig. 6**, we also experimented higher annealing temperature (**Fig. S8**), but the results indicate either growth of larger crystals or re-evaporation of film materials, leading to destruction of the quasi-2D morphology.

The comprehensive microscopy technique employed in this study, including optical microscopy, crossed-polarizer optical microscopy, SEM, and AFM, provides valuable insights into how the macroscopic polarization of the films depends on their microstructure. At deposition temperature, the amorphous phase dominates, which is expected to exhibit a paraelectric behavior. After deposition, as the film warms up to room temperature and crystallizes, the porous spherical dendrites become dominant. The effect of porosity on macroscopic polarization can be

demonstrated using a double layer model (**Fig. S9**)[25]. This model reveals significantly reduced dielectric constants and polarization compared to the single crystal. The post-deposition annealing is crucial for converting disordered porous microstructures into dense spherulites. These spherulites are expected to exhibit dielectric constant and remanent polarization that are close to the single crystal values. However, the maximum P_r found (approximately 0.2 μC/cm^2) is still substantially lower than that of the single crystals. One possible reason is that the polar (001) axis is mostly aligned along the out-of-plane direction [**Fig. 4(e)**], while the P-V measurements are in-plane.

Ultimately, not all materials exhibit spherulite growth[21]. However, we can summarize some general guidelines for processes that optimizes macroscopic ferroelectric properties: (1) low-temperature deposition for quasi-2D morphology and amorphous phase, and (2) post-growth annealing at moderate temperature for controlled crystallization. This process leads to dense microstructures without breaking the quasi-2D morphology. The critical insight from this study lies in recognizing the importance of achieving high microstructure density.

Conclusion

Our investigating focused on the growth of DC-MBI films using the LDRC method, varying deposition temperatures, thickness, and post-deposition annealing. We observed a diverse mix of microstructures, including dense spherulites, porous spherical dendrites, and even more porous randomly oriented fibers. Even with the deposition temperature optimized for spherulite populations, thicker films predominantly exhibited spherical dendrites. However, annealing at a moderate temperature transforms these dendrites into spherulites, which then demonstrate macroscopic ferroelectric polarization switching. The relatively small remanent polarization can be attributed to the preferred orientation of the polar axis along the out-of-plane direction while the measurements are in-plane. These results underscore the significance of microstructure density alongside the quasi-2D morphology in the fabricating films with desirable macroscopic ferroelectric properties. The approach we have established here, i.e., low-temperature deposition followed by controlled crystallization at moderate temperature, is likely applicable to most molecular ferroelectric films.

Methods:

We deposited micro-meter thick DC-MBI films using Angstrom Engineering's Physical Vapor Deposition (EvoVac) within a vacuum setting (~10^{-7} Torr) under thermal evaporation. The modified tool's schematic diagram is shown on **Fig. 1**. Deposition at reduced pressure enabled us to reach the sublimation point (~130°C) before the melting point (~240°C) of DC-MBI, achieving an average deposition rate of ~0.48 A/s. These films were deposited on glass substrates with interdigitated (IDE) Pt electrodes (G-IDEPT5, Metrohm, US) with a period of 10 μm (gap of 4 μm) (**Fig. S10**). The electrodes were connected to a Radiant Precession RT66C Ferroelectric Tester system for real-time in situ electrical measurements. The deposition was carried out at room temperature and at various cryogenic temperatures controlled by a Lakeshore Temperature control system with liquid nitrogen circulation to attain cryogenic conditions. The Quartz Crystal Monitor

(QCM) integrated into the deposition system continuously monitored real-time film thickness. The actual thickness was calibrated later using a couple of test deposited samples, deviating from the nominal thickness by ~100 nm. The spherulitic characteristics of the samples were assessed using a reflective cross-polarized Nikon Eclipse L200N microscope. Micro-scale topographical features were examined using a Keyence Laser Scanning Microscope, while nano-scale features were investigated using ScanAssyst Peak Force Tapping Mode on a Bruker Icon Atomic Force Microscope (AFM). Post-processing annealing of samples in an ambient environment was conducted using a Furnace 1200 Oven. Bruker's D8 2D detector was used as the diffractometer.

Acknowledgements:

This research was primarily supported by the U.S. Department of Energy (DOE), Office of Science, Basic Energy Sciences (BES), under Award No. DE-SC0019173. The work is also supported in part by the Nebraska Center for Energy Sciences Research (NCESR). The research was performed in part at the Nebraska Nanoscale Facility: National Nanotechnology Coordinated Infrastructure and the Nebraska Center for Materials and Nanoscience, which are supported by the NSF under Grant No. ECCS-2025298 and the Nebraska Research Initiative.

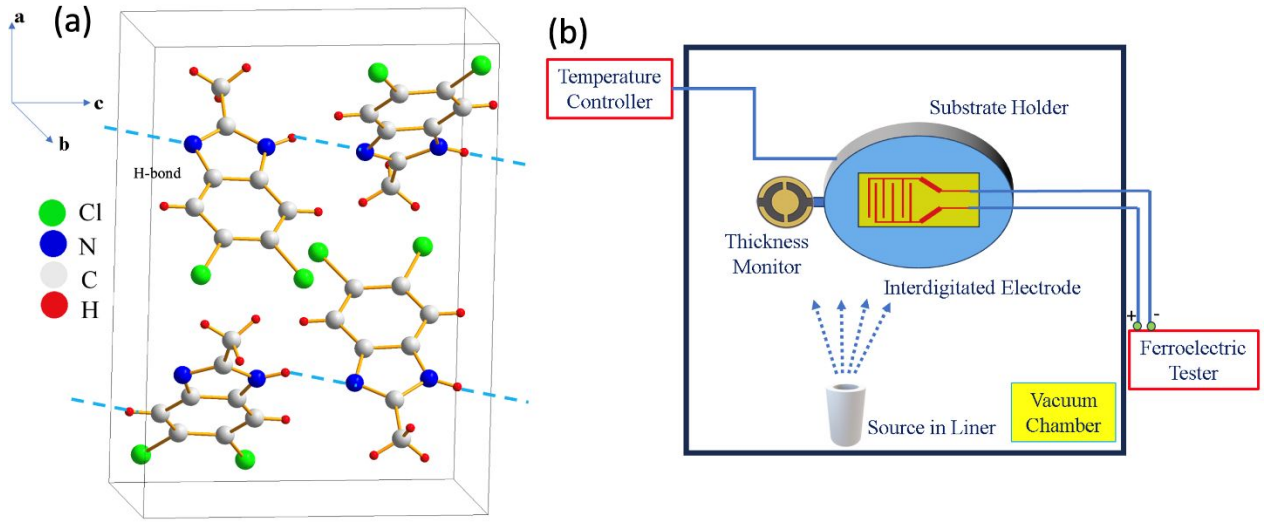

Figure 1. (a) shows the unit cell of the DC-MBI crystal structure with hydrogen bonding pointed along c-axis shown in dotted form. **(b)** shows the schematic experimental setup for the low-temperature deposition –cooling condition is maintained through the continuous supply of liquid nitrogen.

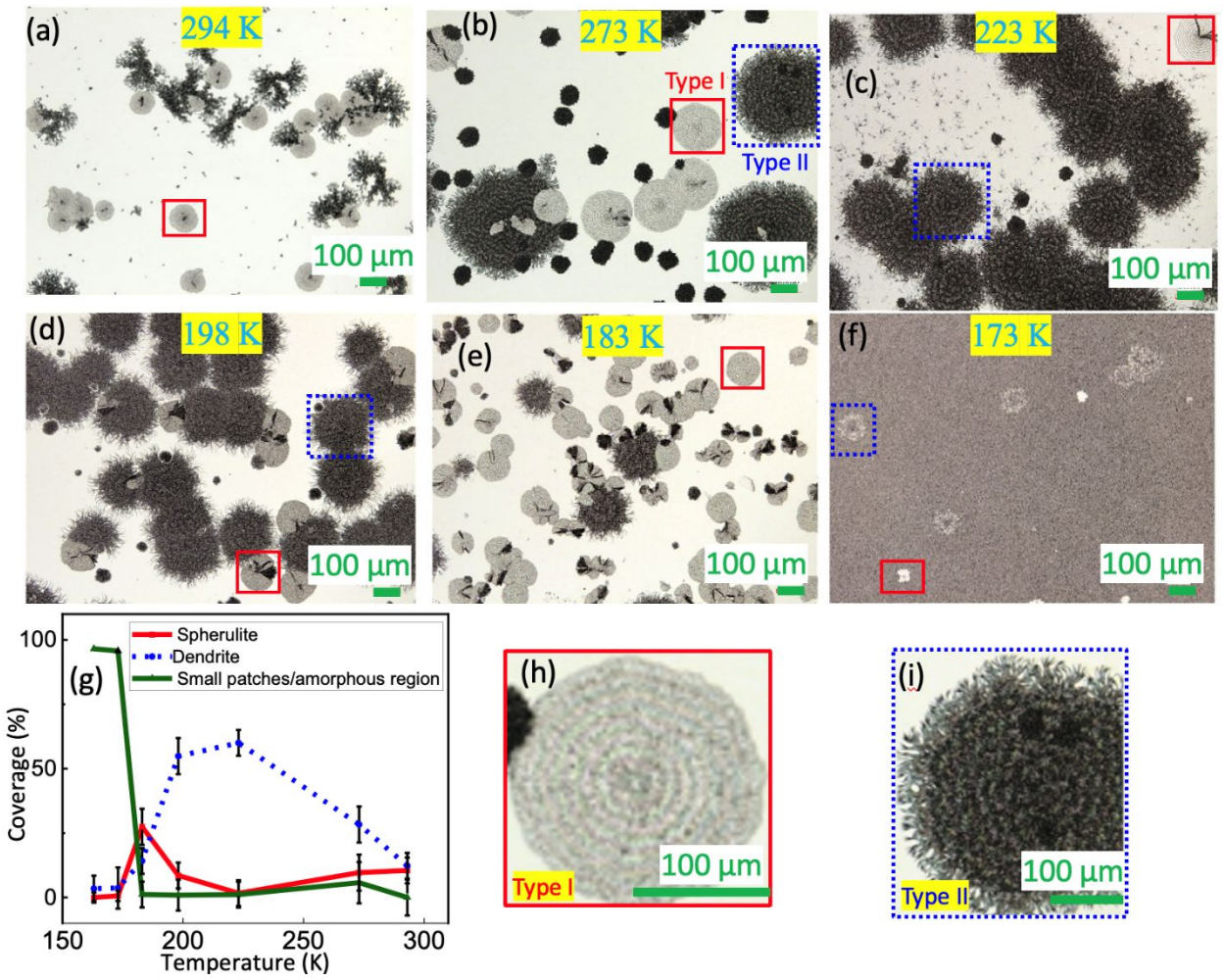

Figure 2. Laser Microscope images for 1µm thickness on (001) Sapphire at various substrate temperatures: 294 K (**a**), 273 K (**b**), 223 K (**c**), 198 K (**d**), 183 K (**e**), 173 K(**f**). At 163 K and below we find optical morphology like (**f**). **(g)** Percentage coverage of spherulite, dendrite and other regions for different T_s samples. **h & i** are closeup laser microscope images for Type-I and Type-II features.

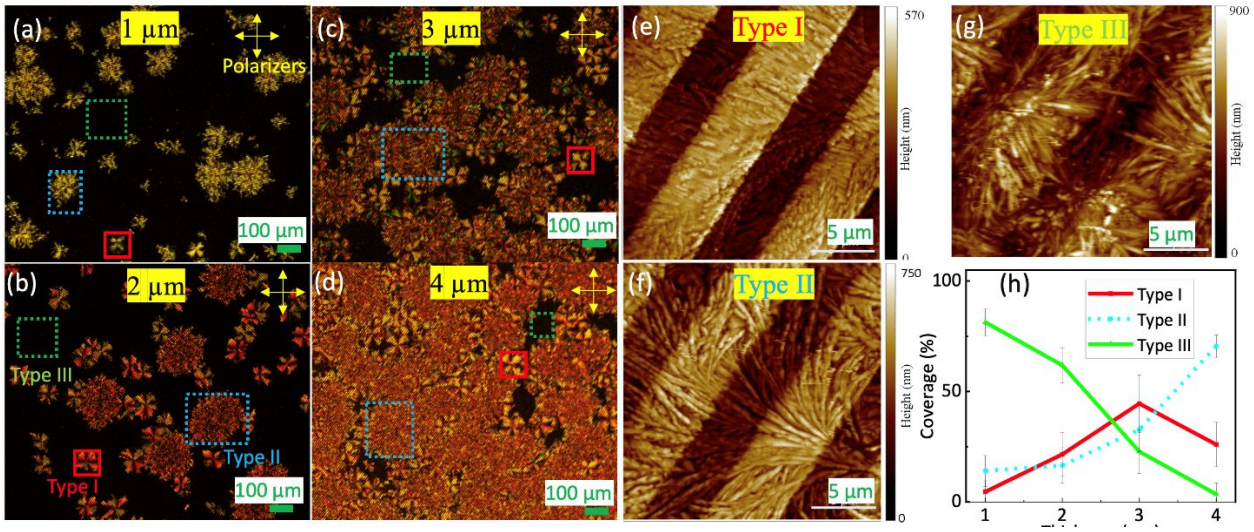

Figure 3. (**a-d)** represents crossed polarized images over IDE substrates for thickness 1 µm, 2µm, 3µm and 4 µm respectively. (**e-g)** shows the AFM images over the IDE for Type-I, Type-II and Type-III features. **h** shows the thickness dependence of three typical areas labeled as I (Spherulite), II and III on **Fig. 2(b).**

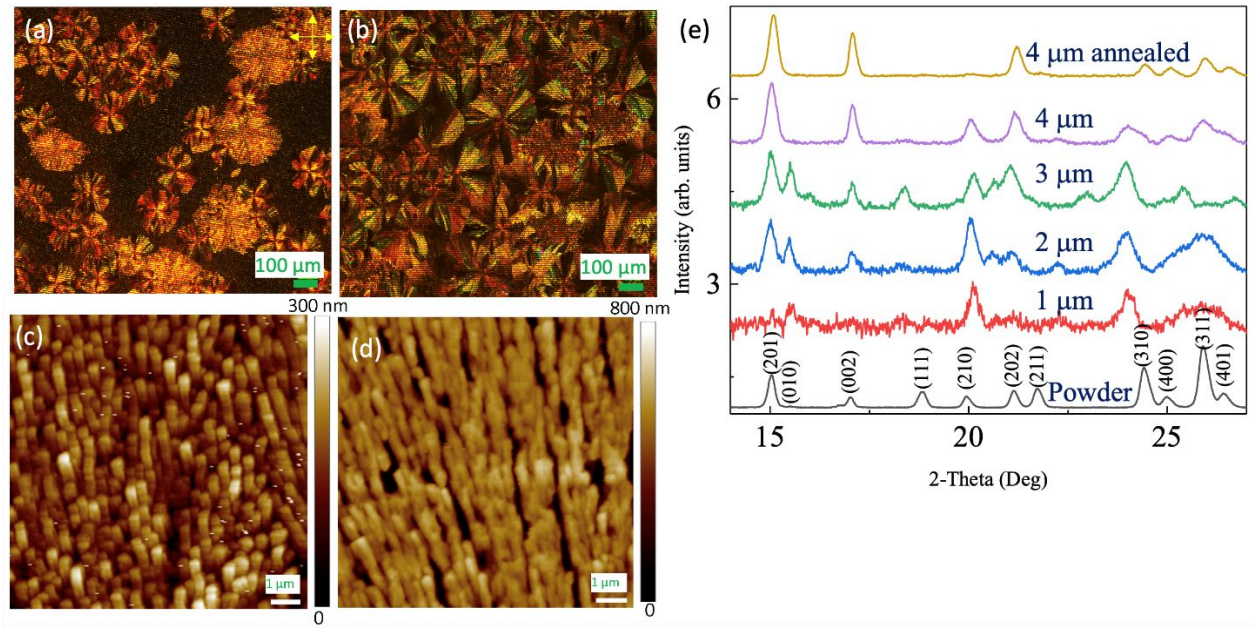

Figure 4. Effect of annealing DC-MBI films. (**a, b)** shows cross polarized image of 4 µm grown sample on bare IDE substrate before and after annealing (not on exact same area but is typical behavior) at 80 C respectively. (**c, d)** shows AFM images over the part of the spherulite before and after annealing. **(e)** XRD for the powder and as grown 1 µm, 2 µm, 3 µm, 4 µm, and 4 µm annealed samples; all data is consistently collected for 1 hr. on Bruker's D8.

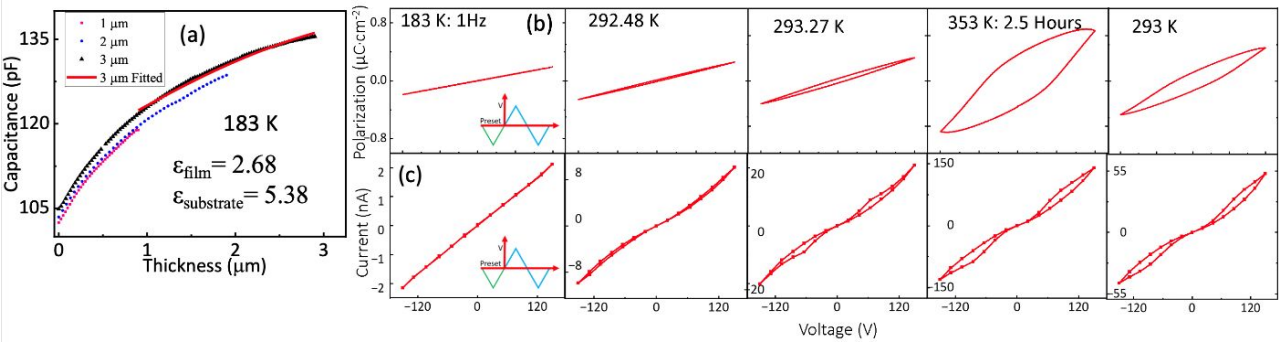

Figure 5. (a) Thickness dependence of IDE capacitive response at 183 K in the paraelectric phase; graph is fitted based on parallel capacitance model of IDE with the validation of necessary criterion[24]. **(b)** IDE device trend during various stages of annealing from 183 K to 353 K and back to room temperature for electrical polarization and current **(c)**.

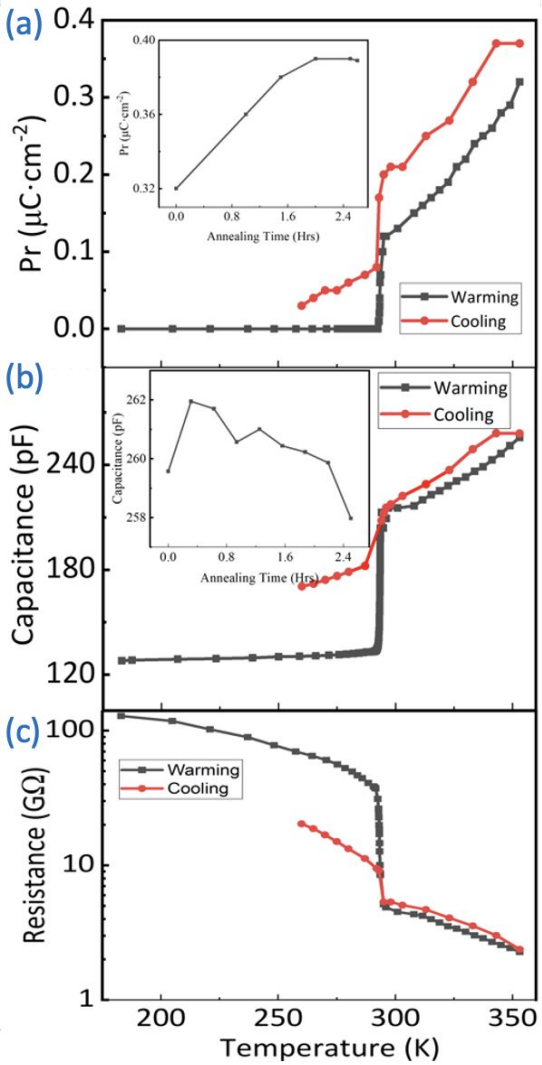

Figure 6. The remanent polarization **(a)**, Capacitance **(b)** and Resistance **(c)** as a function of temperature showing the structural phase transition at 293 K. The thickness of the sample is 4 μm, and the resistance is extracted from I-V curves at 150 V.

References:

1. Owczarek M, Hujsak KA, Ferris DP, et al. Flexible ferroelectric organic crystals. *Nat Commun*. 2016;7. doi:10.1038/ncomms13108
2. Gao W, Chang L, Ma H, et al. Flexible organic ferroelectric films with a large piezoelectric response. *NPG Asia Mater*. 2015;7(6). doi:10.1038/am.2015.54
3. Sugano R, Hirai Y, Tashiro T, et al. Ultrathin flexible memory devices based on organic ferroelectric transistors. *Jpn J Appl Phys*. 2016;55(10). doi:10.7567/JJAP.55.10TA04
4. Jiang X, Lu H, Yin Y, et al. Room temperature ferroelectricity in continuous croconic acid thin films. *Appl Phys Lett*. 2016;109(10). doi:10.1063/1.4962278
5. Horiuchi S, Kobayashi K, Kumai R, Ishibashi S. Proton tautomerism for strong polarization switching. *Nat Commun*. 2017;8. doi:10.1038/ncomms14426
6. Horiuchi S, Tokunaga Y, Giovannetti G, et al. Above-room-temperature ferroelectricity in a single-component molecular crystal. *Nature*. 2010;463(7282):789-792. doi:10.1038/nature08731
7. Zhong W, King-Smith RD, Vanderbilt D. Giant LO-TO splittings in perovskite ferroelectrics. *Phys Rev Lett*. 1994;72(22):3618-3621. doi:10.1103/PhysRevLett.72.3618
8. King-Smith RD, Vanderbilt D. First-principles investigation of ferroelectricity in perovskite compounds. *Phys Rev B*. 1994;49(9):5828-5844. doi:10.1103/PhysRevB.49.5828
9. Neria Y, Neugebauer R. *Bulk Crystal Growth: Basic Techniques, and Growth Mechanisms and Dynamics*. Vol 121.; 2007. Accessed February 14, 2024. http://www.sciencedirect.com:5070/book/9780444633033/handbook-of-crystal-growth
10. Nishinaga T, Rudolph P, Kuech T. Handbook of crystal growth. Accessed February 14, 2024. https://books.google.com/books/about/Handbook_of_Crystal_Growth_2E.html?id=Sr_wrQEACAAJ
11. Yuan Y, Ni Y, Jiang X, Yun Y, Li J, Xu X. Highly Oriented Organic Ferroelectric Films with Single-Crystal-Level Properties from Restrained Crystallization. *Cryst Growth Des*. 2022;22(4):2124-2131. doi:10.1021/acs.cgd.1c01176
12. Yuan Y, Jiang X, Poddar S, Xu X. Electric-field assisted nucleation processes of croconic acid films. *CrystEngComm*. 2019;21(48):7460-7467. doi:10.1039/c9ce01493d
13. Mohapatra S, Beaurepaire E, Weber W, Bowen M, Boukari S, Da Costa V. Accessing nanoscopic polarization reversal processes in an organic ferroelectric thin film. *Nanoscale*.

2021;13(46):19466-19473. doi:10.1039/D1NR05957B

14. Mohapatra S, Da Costa V, Avedissian G, et al. Robust ferroelectric properties of organic croconic acid films grown on spintronically relevant substrates. *Mater Adv*. 2020;1(3):415-420. doi:10.1039/d0ma00147c

15. Hu L, Feng R, Wang J, et al. Space-Charge-Stabilized Ferroelectric Polarization in Self-Oriented Croconic Acid Films. *Adv Funct Mater*. 2018;28(11):1705463. doi:10.1002/ADFM.201705463

16. Horiuchi S, Kagawa F, Hatahara K, et al. Above-room-temperature ferroelectricity and antiferroelectricity in benzimidazoles. *Nat Commun*. 2012;3. doi:10.1038/ncomms2322

17. 2-Methylbenzimidazole, 98%, Thermo Scientific Chemicals, Quantity: 5 g | Fisher Scientific. Accessed February 14, 2024. https://www.fishersci.com/shop/products/2-methylbenzimidazole-98-thermo-scientific-1/AC126330050

18. 5,6-Dichloro-2-methylbenzimidazole 98.0 %, TCI America, Quantity: 1 g | Fisher Scientific. Accessed February 14, 2024. https://www.fishersci.com/shop/products/5-6-dichloro-2-methylbenzimidazole-tci-america-2/D34885G

19. Croconic acid 98 488-86-8. Accessed February 14, 2024. https://www.sigmaaldrich.com/US/en/product/aldrich/391700

20. Crist B, Schultz JM. Polymer spherulites: A critical review. *Prog Polym Sci*. 2016;56:1-63. doi:10.1016/J.PROGPOLYMSCI.2015.11.006

21. Shtukenberg AG, Punin YO, Gunn E, Kahr B. Spherulites. *Chem Rev*. 2012;112(3):1805-1838. doi:10.1021/CR200297F/ASSET/CR200297F.FP.PNG_V03

22. Jonathan A. Dantzig, Michel Rappaz. Solidification - 2nd Edition. 2016;2nd edition. Accessed February 14, 2024. https://press.uchicago.edu/ucp/books/book/distributed/S/bo110496959.html

23. Clarke FW, Thorpe TE, Urbain G. Bi 208.50. Molybdenum.—Müller,2 by oxidation. 1916;2046(1915).

24. Igreja R, Dias CJ. Analytical evaluation of the interdigital electrodes capacitance for a multi-layered structure. *Sensors Actuators, A Phys*. 2004;112(2-3):291-301. doi:10.1016/j.sna.2004.01.040

25. Yun Y, Buragohain P, Thind AS, et al. Spontaneous Polarization in an Ultrathin Improper-Ferroelectric/Dielectric Bilayer in a Capacitor Structure at Cryogenic Temperatures. *Phys Rev Appl*. 2022;18(3):034071. doi:10.1103/PHYSREVAPPLIED.18.034071/FIGURES/4/MEDIUM

26. Park MH, Lee YH, Kim HJ, et al. Ferroelectricity and Antiferroelectricity of Doped Thin HfO2-Based Films. *Adv Mater*. 2015;27(11):1811-1831. doi:10.1002/adma.201404531